IEEE Access
Multidisciplinary | Rapid Review | Open Access Journal

Received November 11, 2019, accepted November 27, 2019, date of publication December 2, 2019,
date of current version December 16, 2019.

*Digital Object Identifier 10.1109/ACCESS.2019.2956983*

# Solid-Electrolyte-Gated Graphene-Covered Metal-Insulator-Silicon-Insulator-Metal Waveguide With a Remarkably Large Modulation Depth

**YONGHAN KIM AND MIN-SUK KWON**
School of Electrical and Computer Engineering, Ulsan National Institute of Science and Technology, Ulsan 44919, South Korea
Corresponding author: Min-Suk Kwon (mskwon@unist.ac.kr)

This work was supported in part by the Basic Science Research Program through the National Research Foundation of Korea (NRF) funded by the Ministry of Science, ICT and Future Planning under Grant NRF-2017R1A2B4007143, and in part by the Samsung Research Funding and Incubation Center for Future Technology under Grant SRFC-IT1901-07.

**ABSTRACT** Silicon photonic modulators are an essential element in providing fast and massive connectivity to the data-centric world. Ever-increasing data usage requires them to be smaller, faster, and easier to fabricate. Graphene with exceptional properties has been emerging as a material for such next-generation silicon photonic modulators, and a variety of graphene-based photonic or plasmonic modulators have been realized and verified. However, due to weak light-graphene interaction in them, they have a modulation depth smaller than 0.16 dB/$\mu$m, which is similar to those of existing germanium-silicon electroabsorption modulators. This work reports a graphene-covered hybrid plasmonic waveguide that has truly strong light-graphene interaction. The hybrid plasmonic waveguide is realized with standard CMOS technology and efficiently coupled to a conventional Si waveguide. To prove the strong light-graphene interaction, solid-electrolyte gating is used to modulate the intensity of the waveguide although its modulation speed is slow. It is demonstrated that the waveguide has a remarkably large modulation depth of 0.276 dB/$\mu$m even though just one single-layer graphene covers the waveguide. This demonstration opens the door to the waveguide covered with a graphene-oxide-graphene capacitor, which may have a larger modulation depth and a large 3-dB bandwidth, and it is theoretically analyzed. This work may be the solid base for a graphene-based silicon photonic modulator which is theoretically expected to surpass current silicon photonic modulators.

**INDEX TERMS** Integrated optics, intensity modulation, nanophotonics, optical waveguides, silicon photonics.

## I. INTRODUCTION

Silicon photonics has firmly established itself as a key enabling technology for datacenters [1] and plays an essential role in handling massive global internet protocol traffic, which will reach 4.8 zettabytes per year by 2022 [2]. Silicon (Si) photonic modulators are an indispensable element in Si photonics. They are usually a Mach-Zehnder interferometer which has two arms tuned by the plasma dispersion effect. They function well up to now, but there are inherent problems: the length of the arms is of the order of 1 mm [3]; their 3-dB bandwidths are lower than 50 GHz [4]. For smaller and faster Si photonic modulators, electro-absorption modulators (EAMs) based on the Franz-Keldysh effect in epitaxially-grown germanium (Ge) or GeSi have been developed [5]–[9]. The EAMs in [7] and [8] have a 40-$\mu$m-long modulation region and a 3-dB bandwidth larger than 50 GHz. However, they have an insertion loss larger than 4.4 dB and a limited optical bandwidth of less than 30 nm. Moreover, EAMs as well as interferometer-type modulators require complex fabrication processes such as ion implantation and high-temperature annealing. In order to deal with ever-increasing data traffic, we still need to make Si photonic modulators even smaller, faster, easier to realize, and work over a wider optical range.

The associate editor coordinating the review of this manuscript and approving it for publication was Nicola Andriolli.

Graphene is the very material that can enable next-generation Si photonic modulators with the desired features since it has exceptional properties such as large carrier mobility, large light absorption, and electrically tunable optical conductivity [10]–[14]. Moreover, graphene-based Si photonic modulators can be made by using much simpler fabrication processes than conventional Si photonic modulators. Therefore, a variety of graphene-based Si photonic modulators have been realized [15]–[23]. A single graphene layer or double graphene layers are placed on a conventional Si waveguide, and graphene interacts with the weak evanescent electric field component of the waveguide mode, which is parallel to graphene. Consequently, the modulation depths of the realized modulators are not dramatically large. For example, Liu *et al*. reported a modulator based on a Si strip waveguide covered with double graphene layers [17], which has the largest modulation depth of 0.16 dB/$\mu$m among the realized graphene-based modulators. In this case, the waveguide should be 28.8 $\mu$m long for the same extinction ratio of 4.6 dB as that of the EAM in [7]. In terms of footprint, hence, graphene-based modulators have not been so superior to conventional EAMs yet. Therefore, for a larger modulation depth, it is imperative to enhance light-graphene interaction as much as possible.

Nanoplasmonic waveguides are effective for strong light-graphene interaction since they can confine light in a region with dimensions below the diffraction limit. Diverse graphene-based nanoplasmonic waveguides have been theoretically investigated, but just a few of them have been realized and verified [24]–[26]. However, the realized waveguides have just a moderate modulation depth smaller than 0.13 dB/$\mu$m which was obtained from a metal slot waveguide covered with double graphene layers [25]. (Although there was a graphene-based nanoplasmonic waveguide with a measured modulation depth of 0.4 dB/$\mu$m, the large value has not been theoretically verified yet [27].) Most of all, it is a serious problem that the realized waveguides resort to fabrication processes incompatible with standard CMOS technology. Therefore, it is necessary to develop graphene-based Si photonic modulators using a nanoplasmonic waveguide which (1) has truly strong light-graphene interaction, (2) is realized with standard CMOS technology, and (3) is efficiently coupled to a conventional Si waveguide. In this paper, we present such a nanoplasmonic waveguide covered with a solid-electrolyte-gated single graphene layer. The focus of this work is to prove that strong light-graphene interaction is obtained from the nanoplasmonic waveguide although it is slowly modulated due to the nature of solid electrolytes. We show experimentally that it has a considerably large modulation depth of 0.276 dB/$\mu$m, which proves its strong light-graphene interaction. Its modulation depth is theoretically verified and repeatedly reproduced. Based on this result, we analyze and discuss the characteristics of a silicon photonic modulator using the nanoplasmonic waveguide covered with a graphene-oxide-graphene capacitor, which may have a larger modulation depth and a large 3-dB bandwidth. The nanoplasmonic waveguide may pave the way for graphene-based Si photonic modulators surpassing conventional Si photonic modulators.

## II. STRUCTURE AND REALIZATION

The nanoplasmonic waveguide used here is a hybrid plasmonic waveguide [28]–[31] named metal-insulator-silicon-insulator-metal (MISIM) waveguide. MISIM waveguides have been actively studied for various applications [32]–[37]. The MISIM waveguide in this study consists of a narrow Si strip and copper (Cu) blocks laterally sandwiching the Si strip with thin silicon dioxide ($SiO_2$) layers in between. Its structure is shown in Fig. 1(a), and it is covered with graphene and solid electrolyte. The Si strip is 250 nm high and 160 nm wide; the Cu blocks are 260 nm high; the $SiO_2$ layers are 30 nm thick. The electric field profile of the MISIM waveguide mode, which was calculated by using a mode solver (Mode Solutions, Lumerical Inc.), is shown in Fig. 1(b). For the calculation, graphene was treated as a boundary with a surface current density determined by the graphene conductivity (see Appendix A) [38]. The electric field, which is dominantly polarized in the horizontal direction, is highly enhanced in the $SiO_2$ layers due to the Cu blocks and the Si strip. In addition, the electric field around the graphene portions on the $SiO_2$ layer ends (*i.e*., at $z = 230$ nm) is almost as strong as that in the middle of the $SiO_2$ layer (*i.e*., at $z = 115$ nm). This leads to strong light-graphene interaction, as proved below. Moreover, the MISIM waveguide is fabricated by using standard CMOS technology [31]. Finally, as shown in Fig. 1(a), it is connected to a 450-nm-wide Si strip waveguide through the coupler which is the region where the Si strip is widened from 160 nm to 450 nm over a distance of 600 nm. The loss of the as-fabricated coupler (before graphene transfer) is ~0.5 dB [31]. All these things indicate that the MISIM waveguide possesses the aforementioned qualities required for graphene-based Si photonic modulators.

To make the MISIM waveguide covered with solid-electrolyte-gated graphene, the as-fabricated MISIM waveguide was slightly modified. Then, graphene grown by chemical vapor deposition (CVD) was wet-transferred onto a chip with the MISIM waveguides and patterned into a strip. Electrodes were made, and, finally, the chip was covered with solid electrolyte composed of $LiClO_4$ and poly(ethylene oxide) (PEO) [39] (these post-fabrication processes are explained in more detail in Appendix B). We measured the Raman spectrum of the graphene transferred and patterned on the chip before forming the solid electrolyte (see Appendix C). The intensity ratio of the 2D peak (near 2700 $cm^{-1}$) to the G peak (near 1580 $cm^{-1}$) in the Raman spectrum was 2.49. This means that the graphene used is almost monolayer. Surface images of the chip and a cross-sectional image of the MISIM waveguide are shown in Fig. 1(c) and (d), respectively. The graphene strip on the MISIM waveguides is 30 $\mu$m wide and covers not only the MISIM waveguides but also the couplers and the parts of

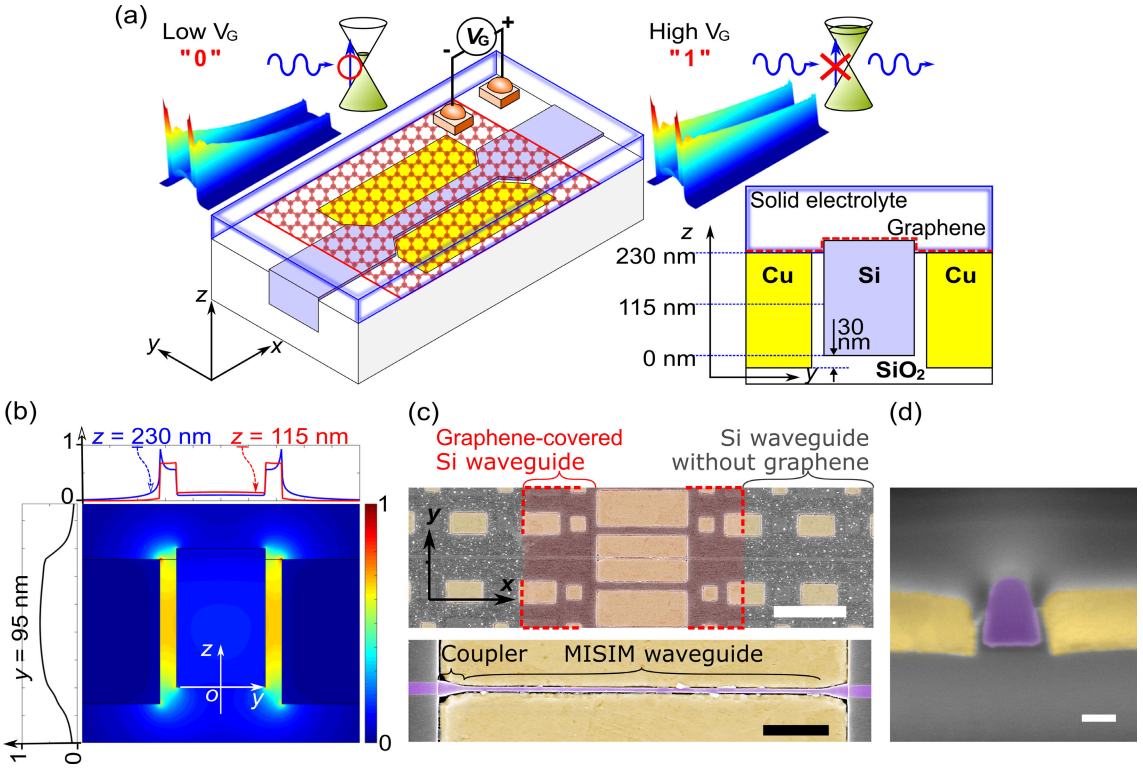


**FIGURE 1.** Structure and images of the MISIM waveguide covered with solid-electrolyte-gated graphene. (a) Schematic diagram and cross-sectional structure of the waveguide. The operation principle of the waveguide is simply explained by using the Dirac cone of graphene and the profile of the time-averaged Poynting vector at $z = 115$ nm in the MISIM waveguide of length 15 $\mu$m. When $V_G$ is low, the chemical potential of graphene, $\mu_c$ is low (*e.g.*, 0.2 eV), and light of wavelength 1550 nm is strongly absorbed by graphene. When $V_G$ is high, $\mu_c$ is high (*e.g.*, 0.6 eV), and the light absorption is prohibited by Pauli blocking. (b) Electric field profile of the MISIM waveguide mode. The field distribution along the $z$ axis at $y = 95$ nm is shown at the left side. The field distributions along the $y$ axis at $z = 115$ nm and 230 nm are shown at the top. (c) False-color surface images of the waveguide. The reddish area is the graphene strip. The scale bars in the upper and lower panels are 10 $\mu$m and 2 $\mu$m, respectively. (d) False-color cross-sectional image of the waveguide. The scale bar is 100 nm.

the Si strip waveguides. If we apply a positive (negative) voltage between the solid-electrolyte and graphene electrodes, electrons (holes) are effectively injected into the graphene strip by positive (negative) ions accumulated on the graphene surface, and the chemical potential of graphene is increased (decreased). When the chemical potential magnitude is larger than half the photon energy, Pauli blocking causes the loss of the waveguide with graphene to decrease to that of the waveguide without graphene (see Fig. 1(a)). In contrast, if the chemical potential is at the Dirac point, the loss is maximum. Since the coupler is covered with graphene, the coupler loss also has ambipolar dependence on the applied voltage as shown below.

## III. EXPERIMENTAL RESULTS

### A. DC CHARACTERISTICS

To obtain the DC characteristics of the MISIM waveguide, changing the applied voltage $V_G$, we measured the propagation loss of the MISIM waveguide and the coupler loss at a wavelength of 1550 nm by using the same method as in [31] (also see Appendix D). The relations of the propagation loss and the coupler loss to $V_G$ are shown in Fig. 2(a) and (b), respectively. The chip contains not only the MISIM waveguides but also the 450-nm-wide Si strip waveguides without the MISIM waveguide. We also measured the propagation loss of the 450-nm-wide Si strip waveguide covered with the solid-electrolyte-gated graphene, which is shown as a function of $V_G$ in Fig. 2(c) (see Appendix D regarding the measurement). In the chip, all the 450-nm-wide Si strip waveguides are connected to 5-$\mu$m-wide Si strip waveguides which are butt-coupled to lensed optical fibers [31]. Actually, we measured the fiber-to-fiber insertion losses (FFILs) of such waveguide combinations. The FFILs of the combinations with the 1-$\mu$m-long and 14-$\mu$m-long MISIM waveguides are shown with respect to $V_G$ in Fig. 2(d). The FFILs seem large since they include two times the coupling loss between the lensed fiber and the 5-$\mu$m-wide Si strip waveguide, the loss of the 5-$\mu$m-wide Si strip waveguides, and the loss of the 450-nm-wide Si strip waveguides (for reference, the FFIL of a combination of the 5-$\mu$m-wide Si strip waveguides and the 4-mm-long 450-nm-wide Si strip waveguide uncovered with graphene is about 20 dB). In addition, the error bars in Fig. 2(d) are quite large: the maximum error bar is $\pm 3.0$ dB. They show the standard deviation of the FFILs of the five combinations separated from each other by 20 $\mu$m. In the case of the as-fabricated MISIM waveguides,

such a standard deviation is usually 1 dB [31]. The increase of the standard deviation may be attributed to nonuniform distribution of graphene residues or the inhomogeneity of the graphene remaining on the chip.

The propagation loss of the MISIM waveguide ($PL_M$) is 0.728 dB/$\mu$m for $V_G = 0$ V and it slightly increases to 0.730 dB/$\mu$m for $V_G = 0.5$ V. If $V_G$ decreases from 0 V or increases from 0.5 V, $PL_M$ decreases. This indicates that the Dirac point of the used graphene is reached for $V_G$ between 0 V and 0.5 V, which is in good agreement with the measurement result of a graphene field effect transistor (see Appendix E). Since $PL_M$ is 0.454 dB/$\mu$m for $V_G = 3$ V, the modulation depth ($MD_M$) is 0.276 dB/$\mu$m when $V_G$ changes from 0.5 V to 3 V; it is significantly large even though just one graphene layer is used. However, $PL_M$ for $V_G = 3$ V is larger than the propagation loss of the as-fabricated MISIM waveguide, which is 0.28 dB/$\mu$m. This may be attributed to an excess loss induced by the modification process [36] and the wet-transfer of graphene. For comparison, using the mode solver, we calculated the relation of $PL_M$ to $V_G$ (see Appendix A regarding the calculation). As shown in Fig. 2(a), the calculated relation is similar to the measured one, and the calculated modulation depth is 0.242 dB/$\mu$m, which is close to the measured value. The discrepancy between the relations exists possibly due to uncertainty in some parameters used for the calculation (see Appendix A).

As shown in Fig. 2(b)-(d), obviously, the coupler loss, the propagation loss of the 450-nm-wide Si strip waveguide, and the FFILs depend on $V_G$ like the propagation loss $PL_M$. The coupler loss for $V_G = 3$ V is 0.5 dB and it is close to the loss of the as-fabricated coupler, which is 0.5 dB. In Fig. 2(c), the propagation loss of the 450-nm-wide Si strip waveguide has a maximum of 0.127 dB/$\mu$m for $V_G = 0.5$ V and decreases to 0.052 dB/$\mu$m as $V_G$ increases to 3 V; the modulation depth of the Si strip waveguide ($MD_S$) is 0.075 dB/$\mu$m. This value is similar to those of previous Si waveguides covered with one graphene layer [16]. The comparison between the propagation losses of the MISIM waveguide and the Si strip waveguide proves that the MISIM waveguide really enables stronger light-graphene interaction than the Si strip waveguide. In Fig. 2(d), the FFIL decrease with the $V_G$ increase from 0.5 V to 3 V is given by $[MD_M \times l_M + MD_S \times (28.8\ \mu\text{m} - l_M) + \Delta CL]$, where $l_M$ is the MISIM waveguide length and $\Delta CL$ is the coupler loss decrease with the $V_G$ increase from 0.5 V to 3 V. The calculated decreases for $l_M = 1$ $\mu$m and 14 $\mu$m are 2.94 dB and 5.66 dB, respectively. They are slightly larger than the decreases of 1.5 dB and 3.8 dB in Fig. 2(d), but the differences are within the range estimated from the deviations of $MD_M$, $MD_S$, and $\Delta CL$.

In order to confirm that such a large modulation depth can be repeatedly achieved, after the characterization of the first chip (chip 1), we made another two chips (chips 2 and 3). The post-fabrication processes used for chip 2 are the same as those for chip 1. However, in the case of chip 3, we made electrodes after the wet-transfer of graphene by using photolithography, e-beam evaporation, and lift-off. Then, we patterned the graphene into a strip. The propagation losses of the MISIM waveguides in

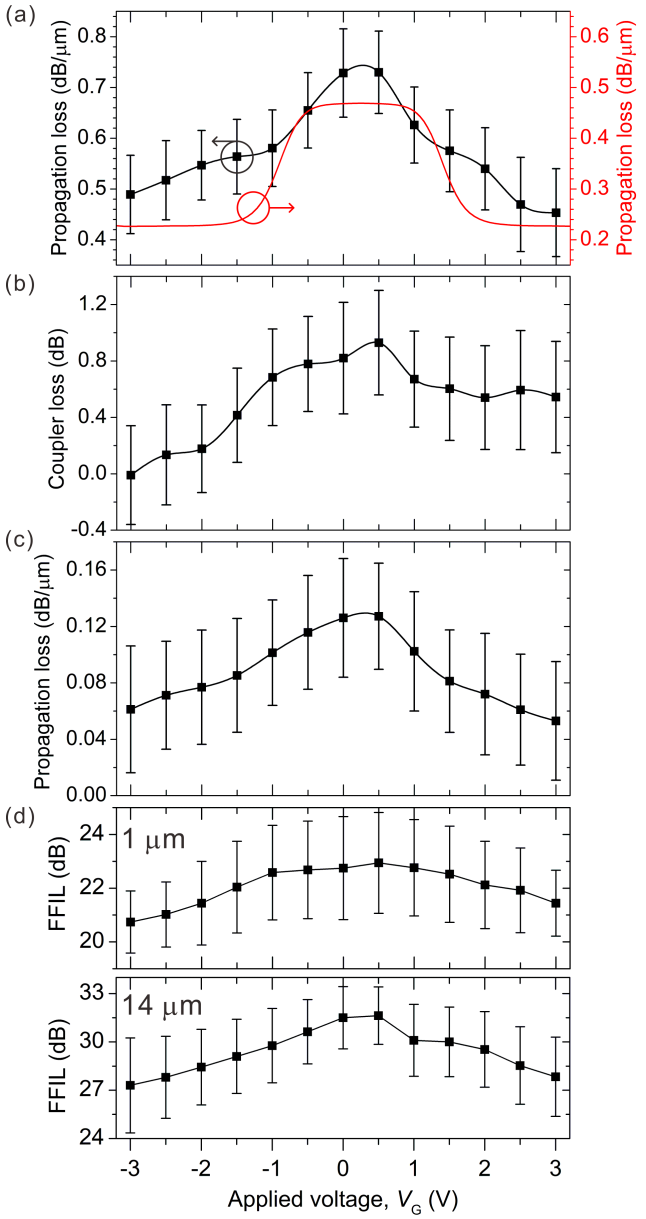


**FIGURE 2.** DC characteristics. (a) Propagation loss of the MISIM waveguide covered with the solid-electrolyte-gated graphene as a function of the applied voltage $V_G$. The red curve shows the calculated relation of the propagation loss to $V_G$. (b) Coupler loss as a function of the applied voltage $V_G$. In panels (a) and (b), the symbols show the measured propagation losses and coupler losses. The error bars represent the standard errors resulting from determining the propagation losses and the coupler losses by linear fitting (see Appendix D). (c) Propagation loss of the 450-nm-wide Si waveguide covered with the solid-electrolyte-gated graphene as a function of the applied voltage $V_G$. The symbol and error bar shows the average and standard deviation of the 25 measured propagation losses at each applied voltage. (d) Fiber-to-fiber insertion loss (FFIL) of the waveguide combination with the MISIM waveguide as a function of the applied voltage $V_G$. The MISIM waveguide is 1 $\mu$m long in the upper panel and 14 $\mu$m long in the lower panel. The symbol and error bar shows the average and standard deviation of the 5 measured FFILs at each applied voltage. In all the panels, the black curves are guides for the eye.

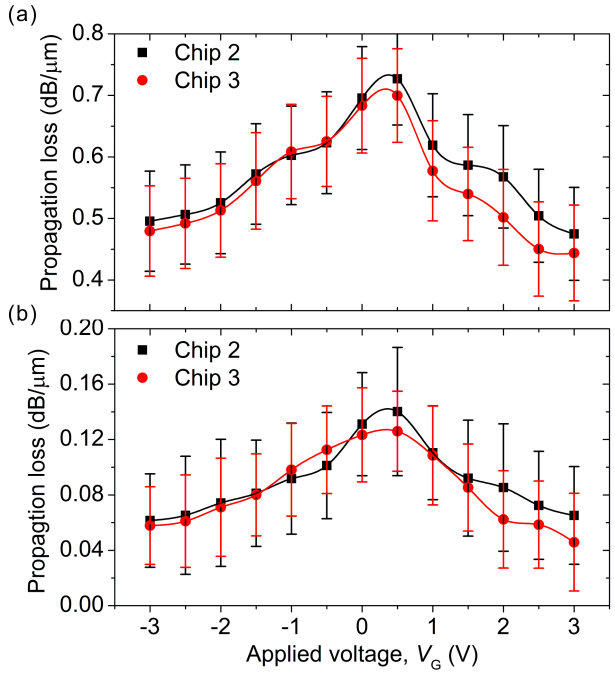


**FIGURE 3.** Propagation losses measured in chips 2 and 3. (a) Propagation losses of the MISIM waveguides covered with the solid-electrolyte-gated graphene in chip 2 and chip 3 as functions of the applied voltage $V_G$. The error bars represent the standard error resulting from determining the propagation loss by linear fitting (see Appendix D). (b) Propagation losses of the 450-nm-wide Si waveguides covered with the solid-electrolyte-gated graphene in chips 2 and 3 as functions of the applied voltage $V_G$. The error bars represent the standard deviation of the 25 propagation losses at each applied voltage (see Appendix D). In panels (a) and (b), the symbols show the measured values, and the solid curves are guides for the eye.

chips 2 and 3 are shown with respect to $V_G$ in Fig. 3(a). In addition, those of the 450-nm-wide Si strip waveguides in chips 2 and 3 are shown with respect to $V_G$ in Fig. 3(b). The modulation depths of the MISIM waveguides in chip 2 and chip 3 are 0.252 and 0.256 dB/$\mu$m, respectively, and those of the 450-nm-wide Si strip waveguides in chips 2 and 3 are 0.075 and 0.08 dB/$\mu$m, respectively. Actually, chips 2 and 3 were made and measured about five months after the measurement of chip 1. This time gap may affect the post-fabrication processes or the solid electrolyte, and the small differences in the modulation depths may be caused by this time gap. Despite the small differences, the results from chips 2 and 3 show that the large modulation depth of the MISIM waveguide is quite reliably reproducible. We also measured the wavelength-dependence of the modulation depths of the MISIM waveguides in chips 2 and 3, which are shown with respect to the wavelength in Fig. 4. In the wavelength range of 1520 to 1630 nm, both the modulation depths change between 0.25 and 0.26 dB/$\mu$m. If the optical bandwidth of an electroabsorption modulator is defined as the wavelength range in which its extinction changes by less than 0.1 dB from the extinction at a reference wavelength (*e.g.*, 1550 nm), the optical bandwidth of the MISIM waveguide covered with the solid-electrolyte-gated graphene is more than 110 nm for an extinction ratio of 4.6 dB.

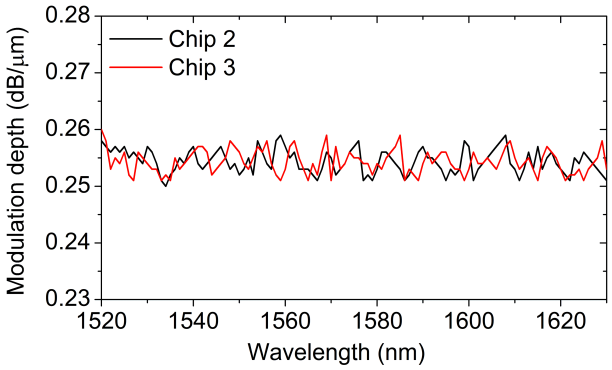


**FIGURE 4.** Wavelength dependence of the modulation depth. The modulation depths measured in chips 2 and 3 are shown as functions of the wavelength.

The large modulation depth in chip 1 can make the MISIM waveguide have an extinction ratio of 4.6 dB when it is 16.7 $\mu$m long (*i.e.*, more than two times shorter than the EAM in [7]). In this case, its loss for $V_G = 3$ V, which is usually defined as its insertion loss, is calculated to be 7.6 dB (3.96 dB) from the measured (theoretical) propagation loss. To reduce the experimental insertion loss, we need to improve the modification process and the transfer process. The insertion loss can be ultimately reduced further if we increase the modulation depth by using double graphene layers as discussed in Section IV.

### B. MODULATION CHARACTERISTICS

Based on the DC characteristics, we observed the modulation characteristics of the MISIM waveguide covered with the solid-electrolyte-gated graphene in chip 1. While applying a sinusoidal voltage signal between the solid-electrolyte and graphene electrodes, we measured the modulated FFIL of the combination with the MISIM waveguide of length 10 $\mu$m. The applied signal oscillated between 1 V and 3 V. We increased the frequency of the signal from 10 Hz to 1 MHz in steps of a factor of 10. Since solid-electrolyte gating is usually slow [40], we used such low frequencies. Fig. 5(a) shows the modulated FFIL along with the modulation signal of frequency 100 kHz. In this case, the modulated FFIL almost synchronizes with the modulation signal. However, in the case that the frequency is 1 MHz, as shown in Fig. 5(b), the modulated FFIL is clearly delayed, and its amplitude decreases as compared to that in Fig. 5(a). Sinusoidal curves with frequencies of 100 kHz and 1 MHz were fitted to the FFIL curves. The electro-optic $S_{21}$ parameter of the waveguide is determined by subtracting the FFIL decrease (in dB) caused by the applied DC voltage increasing from 1 V to 3 V from the peak-to-peak change (in dB) in the fitted curve. The relation of the $S_{21}$ parameter to the frequency is shown in Fig. 5(c). Such a relation obtained from chip 3 is provided in Appendix F. The relations resemble the frequency response of a first- order low-pass filter whose transfer function is given by $1/[1 + j(f/f_{3dB})]$ (the resemblance is clearly checked in

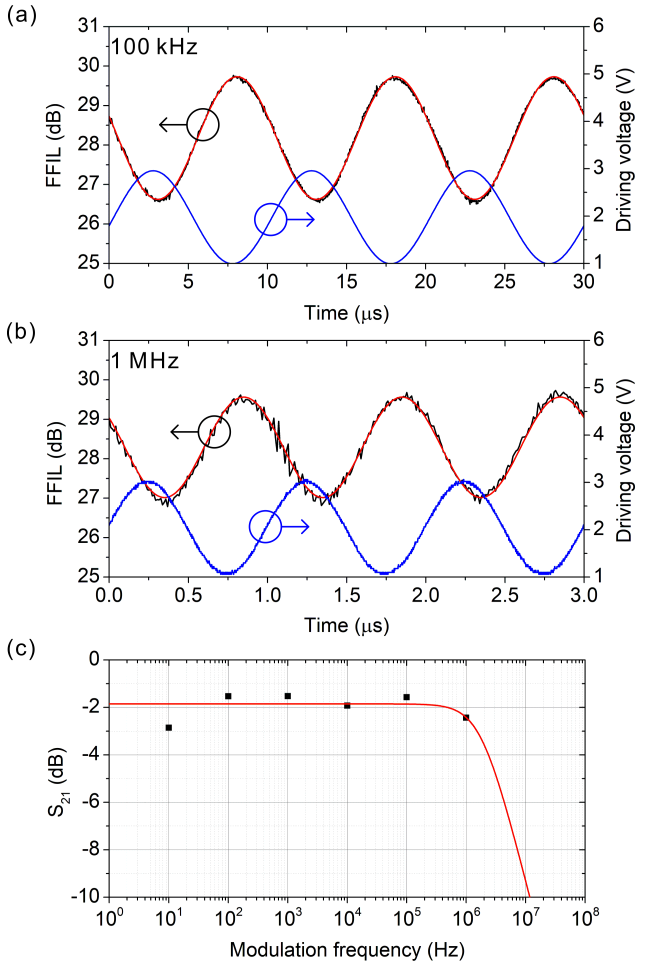


**FIGURE 5.** Modulation characteristics. (a) and (b) Modulated fiber-to-fiber insertion losses (FFILs) of the waveguide combination with the 10-$\mu$m-long MISIM waveguide. In panels (a) and (b), the frequency of the sinusoidal modulation signal is 100 kHz and 1 MHz, respectively. The black curves show the modulated FFILs, and the red curves show the sinusoidal curves fitted to them. For reference, the blue curves show the modulation signals. (c) Relation of the electro-optic $S_{21}$ to the modulation frequency. The symbols show the $S_{21}$ values which are determined by the peak-to-peak amplitudes of the modulated FFILs. The red curve is the transfer curve of a first-order low-pass filter, which was fitted to the relation of $S_{21}$.

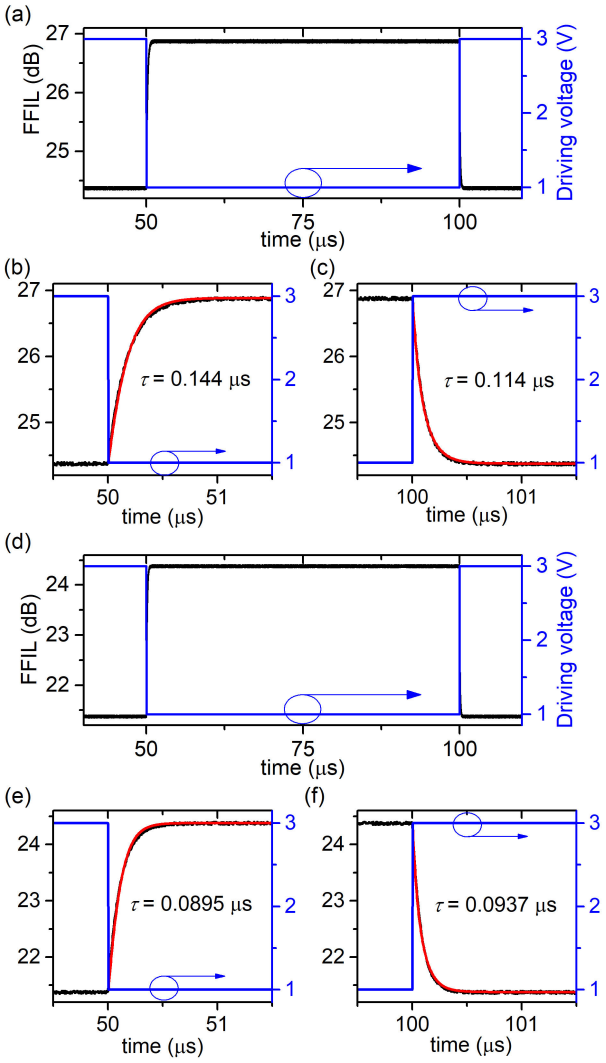


**FIGURE 6.** Modulation by a square wave voltage signal of frequency 10 kHz. (a) and (d) Modulated FFILs of the combinations with the MISIM waveguide of length 10 $\mu$m in chips 2 and 3 (black curves). (b) and (e) Rising edges of the FFIL curves in (a) and (d). The red curves, calculated with an expression $-10\log_{10}\{\Delta P \times \exp(-(t-t_0)/\tau)+P_0\}$, were fitted to the measured curves. (c) and (f) Falling edges of the FFIL curves in (a) and (d). The red curves, calculated with an expression $-10\log_{10}\{\Delta P[1-\exp(-(t-t_0)/\tau)]+P_0\}$, were fitted to the measured curves.

Appendix F). The transfer curve given by $10\log_{10}[1+(f/f_{3\mathrm{dB}})^2]$ was fitted to the relation in Fig. 5(c). From the transfer curve, the 3-dB bandwidth $f_{3\mathrm{dB}}$ of the waveguide is estimated to be 1.82 MHz. At a frequency near $f_{3\mathrm{dB}}$, the electrical signal and the modulated optical signal have a phase difference estimated with the transfer function in the frequency domain. This phase difference appears as the delay in Fig. 5(b).

To confirm the 3-dB bandwidth, we also measured the FFIL modulation of the combinations with the MISIM waveguide of length 10 $\mu$m in chips 2 and 3 by a square wave voltage signal applied between the electrodes. The applied signal oscillated between 1 V and 3 V. The modulated FFILs are shown in Fig. 6. To determine the time constant $\tau$ of each modulation, we fitted a curve calculated with an expression $-10\log_{10}[\Delta P \times \exp(-(t-t_0)/\tau)+P_0]$ to the rising edge of each FFIL curve. In addition, we fitted a curve calculated with an expression $-10\log_{10}\{\Delta P \times [1-\exp(-(t-t_0)/\tau)]+P_0\}$ to the falling edge of each FFIL curve. In the case of the combination in chip 2, the time constants from the rising and falling edges are 0.144 $\mu$s and 0.114 $\mu$s, respectively. In the case of the combination in chip 3, those are 0.0895 $\mu$s and 0.0937 $\mu$s, respectively. Since the 3-dB bandwidth is given by $1/(2\pi\tau)$, it is estimated to be 1.11 or 1.40 MHz for the combination in chip 2 and 1.78 or 1.70 MHz for the combination in chip 3. These values are similar to that obtained from Fig. 5(c). Actually, the rising and falling edges are caused by the dissipation and formation of an electric double layer (EDL) in the solid electrolyte, respectively,

and the difference between their time constants is related to the hysteresis of solid-electrolyte gating [41]. As shown in Appendix F, the relation of the FFIL to $V_G$ increasing from 0 V to 3 V is slightly different from that of the FFIL to $V_G$ decreasing from 3 V to 0 V. However, the hysteresis is small, and this is probably why the modulated FFIL curves in Fig. 5(a) and (b) match well the ideal sinusoidal curves.

On one hand, the 3-dB bandwidth is small since the EDL formation and dissipation of the solid electrolyte is inherently slow [41] and the solid-electrolyte and graphene electrodes are 1 mm distant from each other. In other words, the 3-dB bandwidth is determined by the solid-electrolyte response. However, on the other hand, the modulation is much faster than other operations driven by solid-electrolyte gating since the observed time constants are much smaller than EDL dissipation time (∼10 ms) and EDL formation time (1∼100 s) [41]. One possible reason for this is that the solid electrolyte could be affected by the high humidity during the measurement [42], [43].

## IV. GRAPHENE-CAPACITOR-COVERED WAVEGUIDE

Up to this point, we have confirmed that the MISIM waveguide covered with graphene is really useful for a modulator with a large modulation depth. This may lay the cornerstone of developing the MISIM waveguide covered with a graphene capacitor, which can have a larger modulation depth and, possibly, a much larger 3-dB bandwidth. A Si photonic modulator using the MISIM waveguide covered with a graphene capacitor is schematically shown in Fig. 7(a), and the cross-section of the MISIM waveguide is shown in Fig. 7(b). The graphene capacitor consists of two graphene layers and an aluminum oxide ($Al_2O_3$) layer of thickness $t_{ox}$ ($t_{ox}$ was set at 10 nm). The width of the gap between the electrodes ($w_g$) can be made small since the MISIM waveguide mode is strongly confined in the insulator layers between the Si strip and the Cu blocks. In other words, the electrodes do not affect the MISIM waveguide mode if $w_g$ is larger than about 300 nm. By narrowing the gap, it is possible to decrease the resistance of the graphene layers and the capacitance of the capacitor. This is a clear advantage of the MISIM waveguide. In the case of a conventional Si strip waveguide covered with a graphene capacitor, the gap between two electrodes for such a graphene capacitor should be wider than a few micrometers.

To analyze the modulator, first, we calculated the modulation depth of the MISIM waveguide at a wavelength of 1550 nm. For the calculation, we assumed that the electrodes are infinitely separated and the graphene layers are infinitely wide. The calculated relation of the propagation loss of the MISIM waveguide to the graphene chemical potential $\mu_c$ is shown in Fig. 8(a) (we considered that the chemical potential of the upper graphene layer is $\mu_c$ while that of the lower graphene is $-\mu_c$). As $\mu_c$ increases from 0 eV to 0.6 eV, the propagation loss decreases from 0.649 dB/$\mu$m to 0.237 dB/$\mu$m, and the modulation depth (*i.e.*, the propagation loss decreases due to the $\mu_c$ increases from 0 eV to 0.6 eV) is 0.412 dB/$\mu$m in this case. Next, we determined the

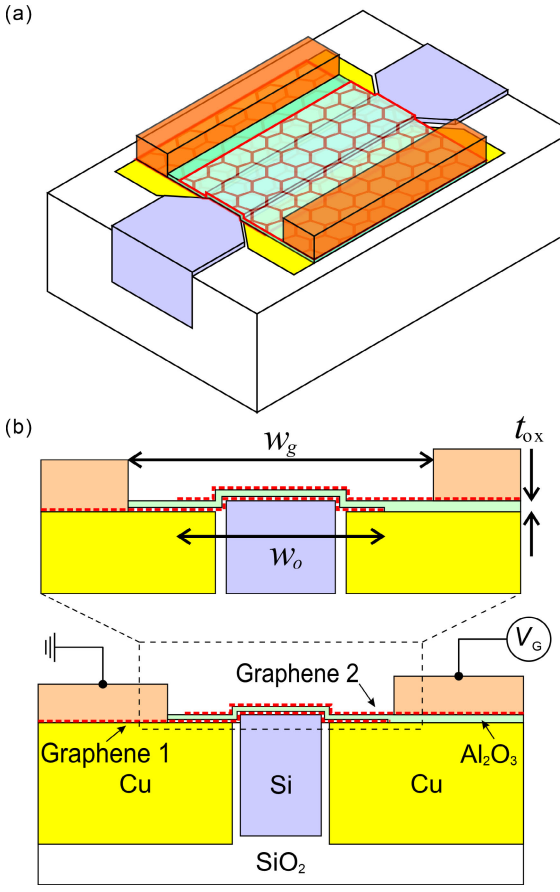


**FIGURE 7.** Structure of the MISIM waveguide covered with a graphene capacitor. (a) Schematic diagram of the device. (b) Cross-sectional structure of the device.

width of the region where the two graphene layers overlap with the $Al_2O_3$ layer in between. The modulation depth is shown as a function of the overlap region width $w_o$ in Fig. 8(b). It almost does not change for $w_o > 300$ nm, and $w_o$ was set at 300 nm. Finally, the electrode gap width $w_g$ was set at 800 nm. The theoretical modulation depth of 0.412 dB/$\mu$m may be undoubtedly achieved from a realized device since the realized MISIM waveguide covered with single-layer graphene really has the modulation depth similar to the calculated value.

For an extinction ratio of 4.6 dB, which is that of the Ge electroabsorption modulator in [7], the MISIM waveguide should be 11.2 $\mu$m long. Then, the total length of the modulator including the two couplers is 12.4 $\mu$m, and the insertion loss of the modulator is 3.65 dB. The 3-dB bandwidth of the modulator can be estimated in the following way. Under the assumption that the 3-dB bandwidth is limited by the *RC* time constant, we determined the device resistance $R$ and capacitance $C$ of the modulator. When the sheet resistance of graphene and the contact resistance between the electrode and graphene are denoted by $r_s$ and $r_c$, respectively, the device resistance is given by $R = [2r_c + r_s \times (w_g + w_o)] / l_g$, where $l_g$ is the MISIM waveguide length ($l_g = 11.2\mu$m). For $r_s = 125\Omega$/sq [44] and $r_c = 100\Omega \cdot \mu$m [45],

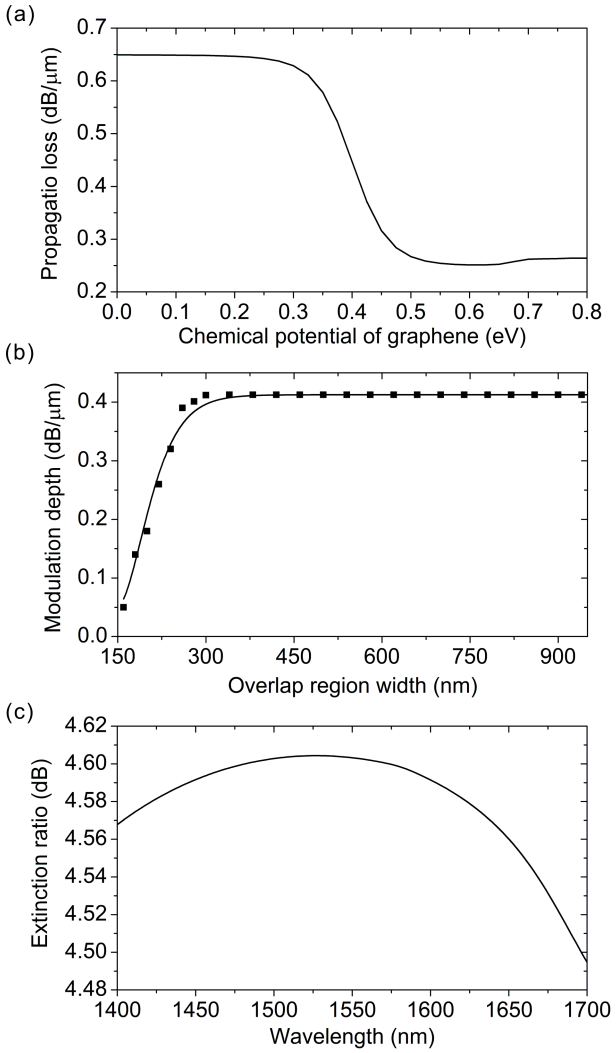


**FIGURE 8.** Characteristics of the MISIM waveguide covered with the graphene capacitor. (a) Relation of the propagation loss to the graphene chemical potential. (b) Relation of the modulation depth to the overlap region width ($w_o$). (c) Relation of the extinction ratio of the modulator to the wavelength.

$R = 30.2\Omega$. When the quantum capacitance of graphene and the capacitance of the graphene overlap region are denoted by $C_q$ and $C_o$, respectively, the device capacitance is given by $C = (1/C_o + 2/C_q)^{-1}$. $C_q$ is approximately given by $2e^2\mu_c l_g w_g/(\pi\hbar^2 v_F^2)$ [46], and the gate capacitance $C_o$ is given by $\varepsilon_0\varepsilon_r l_g w_o / t_{ox}$. In the expressions, $e$ and $\hbar$ are the electron charge and the reduced planck constant, respectively; $v_F$ is the Fermi velocity, which was set at $1 \times 10^6$ m/s; $\varepsilon_0$ and $\varepsilon_r$ are the vacuum permittivity and the RF dielectric constant of $Al_2O_3$ ($\varepsilon_r = 10.3$), respectively. As $\mu_c$ increases from 0.1 eV to 0.6 eV, $C_q$ increases from 210 fF to 1.26 pF. $C_o$ is 30.5 fF and it is much smaller than $C_q$. Hence, the device capacitance $C$ is dominantly determined by $C_o$. With $C_q$ evaluated for $\mu_c = 0.4$ eV, $C = 28.5$ fF. In consequence, the 3-dB bandwidth, which is given by $(2\pi RC)^{-1}$, is 185 GHz. (Actually, it highly depends on $r_s$ and $r_c$, which depend on fabrication processes. For example, if they are five times larger than used for the estimation, it decreases to 37 GHz.) Finally, we confirmed that the extinction ratio changes by less than 0.1 dB from 4.6 dB in the wavelength range between 1400 nm and 1695 nm (Fig. 8(c)). Therefore, the optical bandwidth of the modulator reaches almost 300 nm.

## V. CONCULSION

We have experimentally investigated the MISIM waveguide covered with the solid-electrolyte-gated single graphene layer. We have demonstrated that it has the largest modulation depth of 0.276 dB/$\mu$m among all the graphene-based waveguide modulators which have been realized and verified up to now. The record-high modulation depth indicates that the MISIM waveguide really enables strong light-graphene interaction. Because of the solid-electrolyte gating and the use of the widely separated electrodes, the MISIM waveguide has a rather small 3-dB bandwidth of 1.82 MHz. The confirmation of the large modulation depth almost coincident with the theoretical value increases the likelihood of realizing the MISIM waveguide covered with the graphene capacitor. This MISIM waveguide connected to the input and output Si strip waveguides through the couplers becomes the Si photonic modulator, which theoretically has a smaller length (of 12.4 $\mu$m for an extinction ratio of 4.6 dB), a larger 3-dB bandwidth (of >185 GHz), a larger optical bandwidth (of >300 nm), and a smaller insertion loss (of 3.65 dB) as compared to the previous EAMs [7]. Therefore, this work may open the door to graphene-based Si photonic modulators which really outperform existing Si photonic modulators.

## APPENDIX

### A. CALCULATION

For the simulation of the MISIM waveguide covered with the solid-electrolyte-gated graphene, we used the expression of the graphene conductivity in [38], which is derived from the Kubo formula within the random phase approximation. The relaxation time of graphene, which is necessary for the expression, was set at 25 fs. The carrier mobility of graphene can be estimated by using the Raman spectrum of graphene, which is about 2160 $cm^2$/V/s. In addition, it can be estimated by using the relation of the source-drain resistance of a graphene field-effect transistor to the gate voltage (see Appendix E), which is about 2136 $cm^2$/V/s. When the carrier mobility is around these values, the relaxation time is about 25 fs [47], and we used this value for the simulation. Since the graphene conductivity is a function of the chemical potential of graphene, $\mu_c$, we need to convert the applied voltage $V_G$ to $\mu_c$. For this conversion, we used the simple capacitor model which results in the conversion relation: $V_G - V_{Dirac} = \mu_c e^{-1} + \mathrm{sgn}(\mu_c)\mu_c^2 e(\pi\hbar^2 v_F^2 C_g)^{-1}$ [37]. In this relation, $V_{Dirac}$ is the Dirac point voltage of graphene, which was set at 0.25 V; sgn is the sign function. $C_g$ is the electric double layer capacitance between the graphene and solid electrolyte, and it is given by $\varepsilon_0\varepsilon_r d^{-1}$, where $\varepsilon_r$ and $d$ are the dielectric constant and Debye length of the solid electrolyte, respectively. $\varepsilon_r$ and $d$ are 5.5 [39] and 3 nm (this value was chosen as

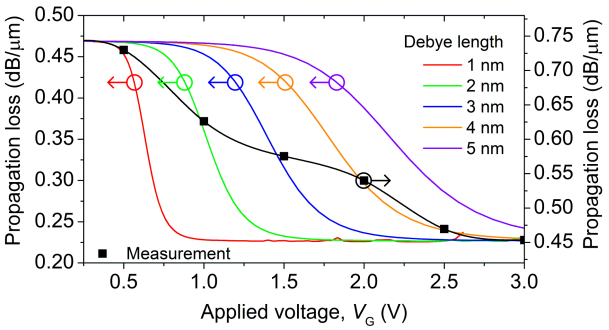


**FIGURE 9.** Influence of the Debye length on the relation of the propagation loss to the applied voltage. Such relations, which were calculated for a few values of the Debye length, are shown along with the measured one.

explained below), respectively, and $C_g$ is 16.2 mF/m$^2$. This value was employed to obtain the curve in Fig. 2(a).

Actually, depending on the relaxation time and the electric double layer capacitance $C_g$, the calculated relation of the propagation loss to $V_G$ changes. We checked that the relaxation time does not affect significantly the relation. However, $C_g$ affects directly the relation via the conversion relation. Since the Debye length $d$ is in the range of 1 to 5 nm [48], there is uncertainty in the actual value of $C_g$. We calculated the relations of the propagation loss to the applied voltage for a few values of the Debye length (Fig. 9). As $C_g$ decreases, the graphene chemical potential becomes smaller for a given value of the gate voltage. In consequence, as the Debye length increases, the rapid decrease of the propagation loss occurs at a larger value of the applied voltage. The measured curve of the propagation loss for $V_G < 1$ V is similar to the curve calculated for $d = 2$ nm. However, the measured curve for $V_G > 2$ V matches well the curve calculated for $d = 4$ nm. It is not clear which value of $d$ should be used unless $d$ is measured or experimentally determined, which is out of the scope of this work. Therefore, $d$ was arbitrarily chosen to be 3 nm for the simulation, and the curve calculated for $d = 3$ nm looks somewhat different from the measured curve. We still need to find out why the propagation loss decreases rather slowly as $V_G$ increases.

### B. FABRICATION PROCESSES

First, as explained in [31], we fabricated the MISIM waveguides on an 8-inch silicon-on-insulator wafer by using a process service provided by National Nanofab Center. The thicknesses of the Si layer and buried oxide of the wafer were 250 nm and 2 $\mu$m, respectively. Identical chips with dimensions of 15 mm$\times$20 mm were made on the wafer. We used just standard CMOS fabrication processes: 248-nm optical lithography, reactive-ion etching (RIE), chemical vapor deposition of dielectrics, sputtering of Cu, and chemical-mechanical polishing. After the fabrication, the wafer was divided into the chips by using a dicing process.

The $SiO_2$ layer originally surrounds the Si strip of the as-fabricated MISIM waveguide above the level of the Cu surface (*i.e.*, $z = 230$ nm). If graphene is transferred on the as-fabricated MISIM waveguide, it cannot interact with the electric field strongly confined between the Si strip and the Cu blocks. Hence, the part of the $SiO_2$ layer above the Cu surface was wet-etched for 5 seconds in a buffered oxide etchant solution (Buffered Oxide Etch 6:1, J. T. Baker). Onto a chip with the MISIM waveguides modified in this way, we wet-transferred graphene (Graphene Square Inc.). For the wet-transfer, we used conventional steps: spin-coating poly(methyl methacrylate) (PMMA, MicroChem Corp.) on graphene on one side of a Cu foil, RIE of graphene on the other side of the Cu foil with $O_2$ and Ar, wet-etching of the Cu foil in an aqueous solution of ammonium persulfate (Sigma Aldrich) (where the weight ratio of ammonium persulfate to water is 1:10), rinsing the PMMA-backed graphene in deionized water for five hours, placing the PMMA-backed graphene on the chip, baking the chip on a hot plate at a temperature of 150 °C for 10 minutes, and removing the PMMA layer by placing the chip in acetone for 12 hours. Completing the wet-transfer, to form a graphene strip, we carried out RIE of the transferred graphene with a photoresist (AZ5214E) mask. After the RIE, we removed the remaining photoresist mask with acetone and made electrodes by using e-beam evaporation of 5-nm-thick titanium and 200-nm-thick gold through a shadow mask. Then, we made SU-8 (SU-8 2015, MicroChem Corp.) protection strips covering the end regions of the 5-$\mu$m-wide Si strip waveguides and diced the chip through the protection strips to prepare the end facets of the chip for the butt-coupling. Finally, we prepared a mixture of $LiClO_4$, poly(ethylene oxide) (PEO), and methanol with a weight ratio of 0.1:1:40 and spin-coated the mixture on the chip and baked the chip on a hot plate at a temperature of 100 °C for 20 minutes.

### C. RAMAN SPECTRA

We measured the Raman spectrum of graphene transferred on a silicon dioxide substrate. In addition, we measured that of graphene transferred on a chip with the MISIM waveguides (not covered with the solid electrolyte). The measured Raman spectra are shown in Fig. 10(a) and (b), respectively, and a microscope image of the chip is shown in Fig. 10(c). The image indicates the position at which the Raman spectrum in Fig. 10(b) was observed. Since the position is on the Cu block, the spectrum has a background signal coming from the Cu block. We calculated the intensity ratio of the 2D peak (near 2700 cm$^{-1}$) to the G peak (near 1580 cm$^{-1}$). The ratios obtained from Fig. 10(a) and (b) are 3.4 and 2.49, respectively. This means that the graphene used in this work is almost monolayer. The full width at half-maximum (FWHM) of the 2D peak of the Raman spectrum in Fig. 10(b) is about 40 cm$^{-1}$. From the correlation between the graphene mobility $\mu$ and the FWHM, which is given by $\mu = 1.3\times10^6\times \exp(-0.16\cdot\text{FWHM})$ [49], $\mu$ is estimated to be 2160 cm$^2$/V/s.

### D. MEASUREMENT METHODS

To measure the propagation loss of the MISIM waveguide and the coupler loss, we input light from a tunable laser to one

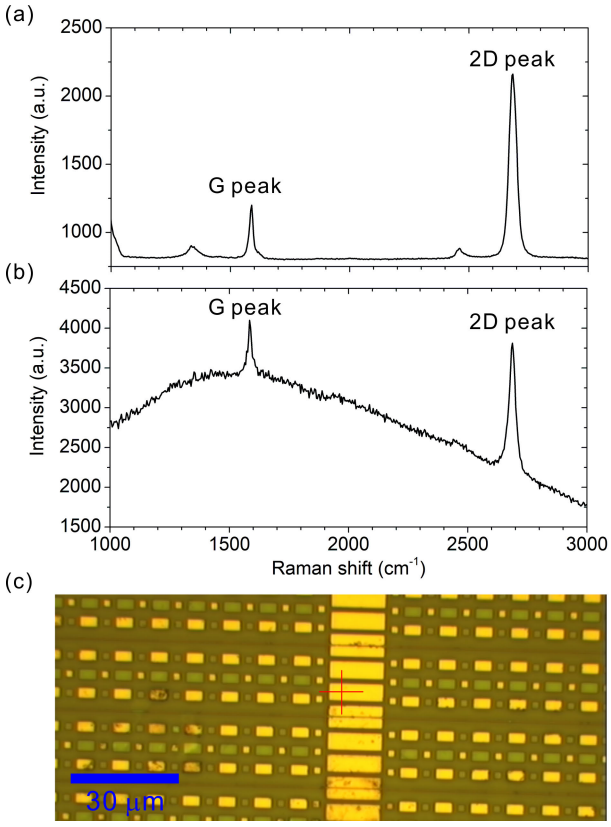


**FIGURE 10.** Measurement of the Raman spectra of graphene. (a) Raman spectrum of the graphene transferred on a silicon dioxide substrate. (b) Raman spectrum of the graphene on a chip with the MISIM waveguides. It has a background signal coming from Cu. (c) Optical microscope image of the chip with the MISIM waveguides covered with graphene. The crosshair indicates the location at which the Raman spectrum in panel (b) was acquired.

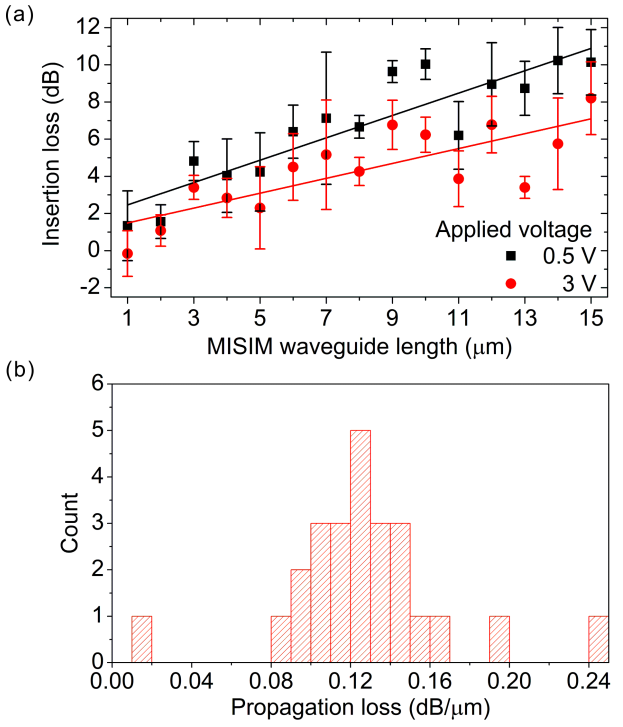


**FIGURE 11.** Propagation loss measurements. (a) Relations between the insertion loss of the MISIM waveguide and the MISIM waveguide length. The symbol and error bar shows the average and standard deviation of the insertion losses of the 5 MISIM waveguides with the same length. The straight lines are fitted to the symbols. (b) Distribution of the propagation losses obtained from the 25 450-nm-wide Si strip waveguides covered with the solid-electrolyte-gated graphene. In this case, the applied voltage $V_G$ is 0 V.

of the combinations of the 5-$\mu$m-wide Si strip waveguides, the 450-nm-wide Si strip waveguides of length 2 mm, and the MISIM waveguide via a lensed fiber. We controlled the polarization of the input light with a fiber polarization controller to excite transverse-electric modes in the waveguides. The output light from the combination was coupled to another lensed fiber connected to an optical power meter. In this way, we measured the fiber-to-fiber insertion losses (FFILs) (in dB) of the combinations with the MISIM waveguide with a length of 1 to 15 $\mu$m. In addition, we measured the FFIL (in dB) of a reference combination of the 5-$\mu$m-wide Si strip waveguides and the 450-nm-wide Si strip waveguide which is 4 mm long and the central part of which is covered with the 30-$\mu$m-wide graphene strip. The insertion loss of the MISIM waveguide is defined as the FFIL of the reference combination subtracted from the FFIL of the combination with the MISIM waveguide. The relations of the insertion loss to the MISIM waveguide length in chip 1 are shown in Fig. 11(a). When a straight line is fitted to such a relation, the slope of the straight line is equal to the difference between the propagation losses of the MISIM and 450-nm-wide Si strip waveguides covered with the solid-electrolyte-gated graphene according to the definition of the insertion loss. Therefore, the propagation loss of the latter was obtained by adding that of the former to the slope. Finally, the vertical intercept of the straight line is equal to two times the coupler loss.

The propagation loss of the 450-nm-wide Si strip waveguide covered with solid-electrolyte-gated graphene was measured in the following way. Each chip has the 450-nm-wide Si strip waveguides without the MISIM waveguide, the central parts of which are covered with the graphene strip. The number of the Si strip waveguides is 25, and the width of the graphene strip varies between 10 and 50 $\mu$m over the Si strip waveguides. In addition to this chip, for reference, we characterized another chip which is covered with just the solid electrolyte without graphene. We measured the FFILs of the combinations of the 5-$\mu$m-wide Si strip waveguides and the 450-nm-wide Si strip waveguide in the chip with graphene (*e.g.*, chip 1) and those of such combinations in the chip without graphene. The propagation loss of the 450-nm-wide Si strip waveguide covered with the solid-electrolyte-gated graphene was obtained by subtracting the FFIL of one combination in the chip without graphene from that of the corresponding combination in chip 1, dividing the difference by the width of the graphene strip covering the 450-nm-wide Si strip waveguide, and averaging those values resulting from the division (Fig. 11(b)).

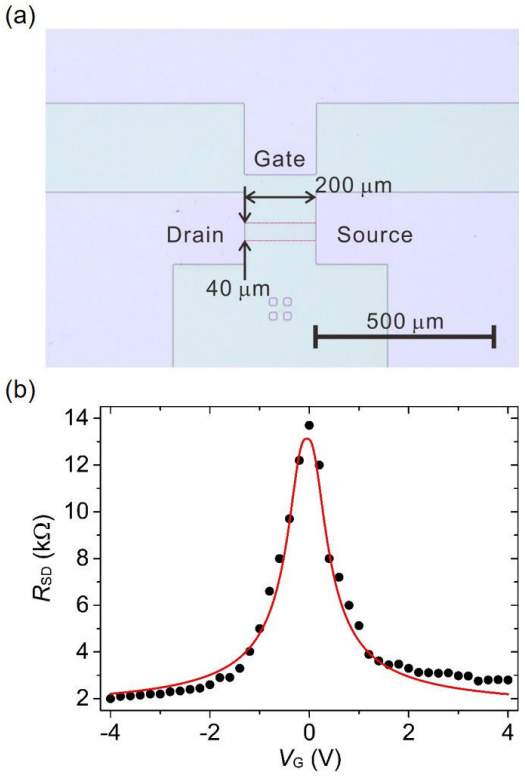


**FIGURE 12.** Graphene field effect transistor. (a) Optical microscope image of the solid-electrolyte-gated graphene field effect transistor (GFET). The graphene channel of the GFET is clarified by the dotted rectangle. (b) Relation between the source-drain resistance $R_{SD}$ and the gate voltage $V_G$. The symbols represent the measured relation, and the solid curve calculated with (A1) is fitted to the measured relation.

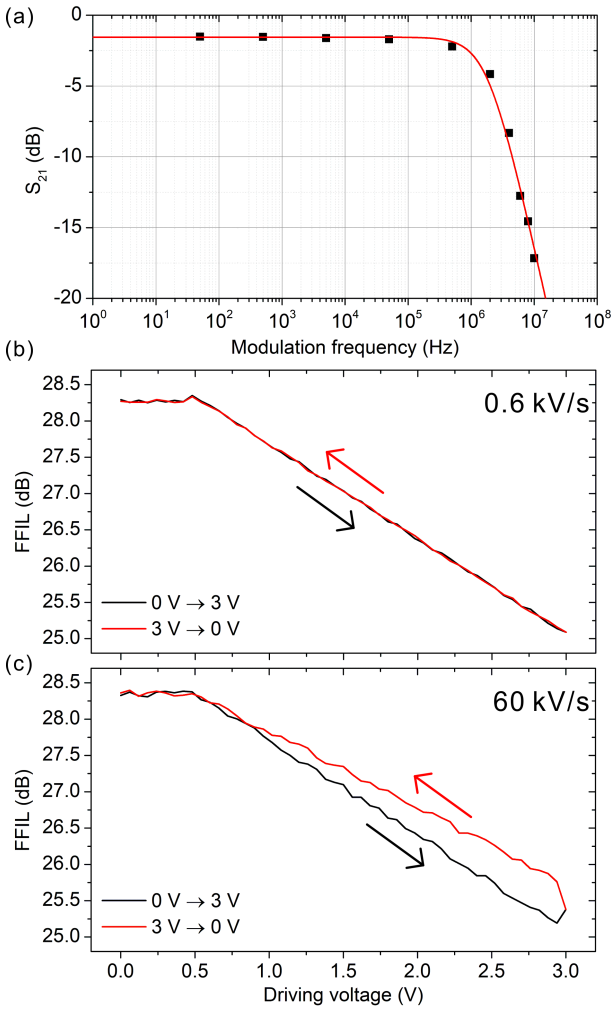


**FIGURE 13.** Additional modulation characteristics measured for the combination with the 10-$\mu$m-long MISIM waveguide in chip 3. (a) Relation of the electro-optic $S_{21}$ to the modulation frequency. The symbols show the measured values of $S_{21}$. The red curve is the transfer curve of a first-order low-pass filter, which was fitted to the relation of $S_{21}$. (b) and (c) Relations of the FFIL of the combination to the driving voltage increasing from 0 V to 3 V (black) and decreasing from 3 V to 0 V (red). The change rate of the driving voltage is 0.6 kV/s and 60 kV/s in (b) and (c), respectively.

### *E. GRAPHENE FIELD-EFFCT TRANSISTOR*

We fabricated a solid-electrolyte-gated graphene field-effect transistor (GFET) on a 200-nm-thick $SiO_2$ layer thermally grown on a Si substrate. We wet-transferred graphene on the $SiO_2$ layer, patterned it, made metal electrodes on the pattern by using a lift-off process, and formed a solid-electrolyte layer on the pattern. A microscope image of the fabricated GFET is shown in Fig. 12(a). The channel of the GFET is 40 $\mu$m wide and 200 $\mu$m long. We measured the resistance between the source and the drain while applying a voltage between $-3$ V and 3 V to the gate while the drain was grounded. The measured resistance $R_{SD}$ is shown as a function of the gate voltage $V_G$ in Fig. 12(b). In [50], the relation between $R_{SD}$ and $V_G$ is approximately given by

$$R_{SD} = R_C + \frac{l}{w}\frac{1}{e\mu}\frac{1}{\sqrt{n_0^2 + n^2}}, \tag{A1}$$

$$n = \frac{1}{e}C_g\overline{V}_G + \frac{\pi}{2}\left(\frac{\hbar v_F}{e^2}\right)^2 C_g^2 - C_g^2\sqrt{\frac{\pi}{e}\left(\frac{\hbar v_F}{e^2}\right)^2\frac{\overline{V}_G}{C_g} + \frac{\pi^2}{4}\left(\frac{\hbar v_F}{e^2}\right)^4}, \tag{A2}$$

$$\overline{V}_G = |V_G - V_{Dirac}|. \tag{A3}$$

In the equations, $R_C$ is the contact resistance of the GFET; $l$ and $w$ are the length and width of the graphene channel, respectively; $\mu$ is the mobility of graphene; $n_0$ is the carrier density at the minimum conductivity, which is generated by charged impurities; $n$ is the carrier density charged by the gate voltage. $R_C$, $\mu$, $n_0$, $C_g$, and $V_{Dirac}$ were determined by fitting (A1) to the measured relation. The parameter values obtained from the fitting are $R_C = 1.5$ kΩ, $\mu = 2135$ cm$^2$/V/s, $n_0 = 1.259 \times 10^{12}$ cm$^{-2}$, $C_g = 9.605$ mF/m, and $V_{Dirac} = -0.0474$ V. The value of $\mu$ is similar to that obtained from the Raman spectrum. As observed from the relation between the gate voltage and the propagation loss of the MISIM waveguide covered with the solid-electrolyte-gated graphene, $V_{Dirac}$ of the graphene on the MISIM waveguide is between 0 and 0.5 V. It is slightly larger than $V_{Dirac}$ in

the case of the GFET. This may be because the graphene is $p$-doped on the Cu blocks [51], [52].

### F. ADDITIONAL MODULATION CHARACTERISTICS

We measured the electro-optic $S_{21}$ parameter related to the 10-$\mu$m-long MISIM waveguide covered with the solid-electrolyte-gated graphene in chip 3 with respect to the frequency. As shown in Fig. 13(a), the transfer curve given by $10\log_{10}[1 + (f/f_{3\mathrm{dB}})^2]$ is in good agreement with the measured curve, and $f_{3\mathrm{dB}}$ is 1.79 MHz.

To check the hysteresis of solid-electrolyte gating, we measured the FFIL of the combination with the 10-$\mu$m-long MISIM waveguide in chip 3 while increasing the driving voltage $V_G$ from 0 V to 3 V and then decreasing $V_G$ from 3 V to 0 V. The measured relations of the FFIL to $V_G$ are shown in Fig. 13(b) and (c), respectively. The increasing and decreasing rate of $V_G$ is 0.6 kV/s in Fig. 13(b) and 60 kV/s in Fig. 13(c). The hysteresis is clearly observed when the rate is quite large.

## REFERENCES


[1] A. F. J. Levi, "Silicon photonics' last-meter problem: Economics and physics still pose challenges to 'fiber to the processor' tech," *IEEE Spectr.*, vol. 55, no. 9, pp. 38–43, Sep. 2018.

[2] Cisco, "Cisco visual networking index: Forecast and trends, 2017–2022 White Paper," Cisco Syst., San Jose, CA, USA, White Paper, May 1975. [Online]. Available: https://www.cisco.com/c/en/us/solutions/collateral/service-provider/visual-networking-index-vni/white-paper-c11-741490.html

[3] D. J. Thomson, F. Y. Gardes, Y. Hu, G. Mashanovich, M. Fournier, P. Grosse, J.-M. Fedeli, and G. T. Reed, "High contrast 40 Gbit/s optical modulation in silicon," *Opt. Express*, vol. 19, no. 12, pp. 11507–11516, May 2011.

[4] J. Ding, R. Ji, L. Zhang, and L. Yang, "Electro-optical response analysis of a 40 Gb/s silicon Mach-Zehnder optical modulator," *J. Lightw. Technol.*, vol. 31, no. 14, pp. 2434–2440, Jul. 15, 2013.

[5] J. Liu, M. Beals, A. Pomerene, S. Bernardis, R. Sun, J. Cheng, L. C. Kimerling, and J. Michel, "Waveguide-integrated, ultralow-energy GeSi electro-absorption modulators," *Nature Photon.*, vol. 2, pp. 433–437, May 2008.

[6] D. Feng, W. Qian, H. Liang, C.-C. Kung, Z. Zhou, Z. Li, J. S. Levy, R. Shafiiha, J. Fong, B. J. Luff, and M. Asghari, "High-speed GeSi electroabsorption modulator on the SOI waveguide platform," *IEEE J. Sel. Topics Quantum Electron.*, vol. 19, no. 6, Nov./Dec. 2013, Art. no. 3401710.

[7] S. A. Srinivasan, M. Pantouvaki, S. Gupta, H. T. Chen, P. Verheyen, G. Lepage, G. Roelkens, K. Saraswat, D. Van Thourhout, P. Absil, and J. Van Campenhout, "56 Gb/s germanium waveguide electro-absorption modulator," *J. Lightw. Technol.*, vol. 34, no. 2, pp. 419–424, Jan. 15, 2016.

[8] S. A. Srinivasan, P. Verheyen, R. Loo, I. De Wolf, M. Pantouvaki, G. Lepage, S. Balakrishnan, W. Vanherle, P. Absil, and J. Van Campenhout, "50 Gb/s C-band GeSi waveguide electro-absorption modulator," in *Proc. Opt. Fiber Commun. Conf. Exhibit. (OFC)*, Anaheim, CA, USA, Mar. 2016, pp. 1–3.

[9] L. Mastronardi, M. Banakar, A. Z. Khokhar, N. Hattasan, T. Rutirawut, T. D. Bucio, K. M. Grabska, C. Littlejohns, A. Bazin, G. Mashanovich, and F. Y. Gardes, "High-speed Si/GeSi hetero-structure electro absorption modulator," *Opt. Express*, vol. 26, no. 6, pp. 6663–6673, Mar. 2018.

[10] F. Bonaccorso, Z. Sun, T. Hasan, and A. C. Ferrari, "Graphene photonics and optoelectronics," *Nature Photon.*, vol. 4, no. 9, pp. 611–622, Sep. 2010.

[11] Q. Bao and K. P. Loh, "Graphene photonics, plasmonics, and broadband optoelectronic devices," *ACS Nano*, vol. 6, no. 5, pp. 3677–3694, Apr. 2012.

[12] A. N. Grigorenko, M. Polini, and K. S. Novoselov, "Graphene plasmonics," *Nature Photon.*, vol. 6, pp. 749–758, Nov. 2012.

[13] P. Avouris and M. Freitag, "Graphene photonics, plasmonics, and optoelectronics," *IEEE J. Sel. Topics Quantum Electron.*, vol. 20, no. 1, pp. 72–83, Jan. 2014.

[14] D. Akinwande, C. Huyghebaert, C.-H. Wang, M. I. Serna, S. Goossens, L.-J. Li, H.-S. P. Wong, and F. H. L. Koppens, "Graphene and two-dimensional materials for silicon technology," *Nature*, vol. 573, pp. 507–518, Sep. 2019.

[15] M. Romagnoli, V. Sorianello, M. Midrio, F. H. L. Koppens, C. Huyghebaert, D. Neumaier, P. Galli, W. Templ, A. D'Errico, and A. C. Ferrari, "Graphene-based integrated photonics for next-generation datacom and telecom," *Nature Rev. Mater.*, vol. 3, pp. 392–414, Oct. 2018.

[16] M. Liu, X. Yin, E. Ulin-Avila, B. Geng, T. Zentgraf, L. Ju, F. Wang, and X. Zhang, "A graphene-based broadband optical modulator," *Nature*, vol. 474, no. 7349, pp. 64–67, May 2011.

[17] M. Liu, X. Yin, and X. Zhang, "Double-layer graphene optical modulator," *Nano Lett.*, vol. 12, no. 3, pp. 1482–1485, Feb. 2012.

[18] N. Youngblood, Y. Anugrah, R. Ma, S. J. Koester, and M. Li, "Multifunctional graphene optical modulator and photodetector integrated on silicon waveguides," *Nano Lett.*, vol. 14, no. 5, pp. 2741–2746, Apr. 2014.

[19] M. Mohsin, D. Schall, M. Otto, A. Noculak, D. Neumaier, and H. Kurz, "Graphene based low insertion loss electro-absorption modulator on SOI waveguide," *Opt. Express*, vol. 22, no. 12, pp. 15292–15297, 2014.

[20] C. Qiu, W. Gao, R. Vajtai, P. M. Ajayan, J. Kono, and Q. Xu, "Efficient modulation of 1.55 $\mu$m radiation with gated graphene on a silicon microring resonator," *Nano Lett.*, vol. 14, no. 12, pp. 6811–6815, Nov. 2014.

[21] C. T. Phare, Y.-H. D. Lee, J. Cardenas, and M. Lipson, "Graphene electro-optic modulator with 30 GHz bandwidth," *Nature Photon.*, vol. 9, no. 8, pp. 511–514, Jul. 2015.

[22] Y. Hu, M. Pantouvaki, J. Van Campenhout, S. Brems, I. Asselberghs, C. Huyghebaert, P. Absil, and D. Van Thourhout, "Broadband 10 Gb/s operation of graphene electro-absorption modulator on silicon," *Laser Photon. Rev.*, vol. 10, no. 2, pp. 307–316, Jan. 2015.

[23] H. Dalir, Y. Xia, Y. Wang, and X. Zhang, "Athermal broadband graphene optical modulator with 35 GHz speed," *ACS Photon.*, vol. 3, no. 9, pp. 1564–1568, Sep. 2016.

[24] D. Ansell, I. P. Radko, Z. Han, F. J. Rodriguez, S. I. Bozhevolnyi, and A. N. Grigorenko, "Hybrid graphene plasmonic waveguide modulators," *Nature Commun.*, vol. 6, Nov. 2015, Art. no. 8846.

[25] X. Guan, X. Zhu, H. Hu, Y. Ding, S. I. Bozhevolnyi, L. K. Oxenløwe, K. J. Jin, N. A. Mortensen, and S. Xiao, "Efficient electro-optic modulation in low-loss graphene-plasmonic slot waveguides," *Nanoscale*, vol. 9, no. 40, pp. 15576–15581, Sep. 2017.

[26] R. Hao, J. Jiao, X. Peng, Z. Zhen, R. Dagarbek, Y. Zou, and E. Yi, "Experimental demonstration of a graphene-based hybrid plasmonic modulator," *Opt. Lett.*, vol. 44, no. 10, pp. 2586–2589, May 2019.

[27] V. J. Sorger, R. Amin, J. B. Khurgin, Z. Ma, H. Dalir, and S. Khan, "Scaling vectors of attoJoule per bit modulators," *J. Opt.*, vol. 20, no. 1, Dec. 2017, Art. no. 014012.

[28] M. Wu, Z. Han, and V. Van, "Conductor-gap-silicon plasmonic waveguides and passive components at subwavelength scale," *Opt. Express*, vol. 18, no. 11, pp. 11728–11736, May 2010.

[29] I. Goykhman, B. Desiatov, and U. Levy, "Experimental demonstration of locally oxidized hybrid silicon-plasmonic waveguide," *Appl. Phys. Lett.*, vol. 97, no. 14, Oct. 2010, Art. no. 141106.

[30] S. Zhu, T. Y. Liow, G. Q. Lo, and D. L. Kwong, "Silicon-based horizontal nanoplasmonic slot waveguides for on-chip integration," *Opt. Express*, vol. 19, no. 9, pp. 8888–8902, Apr. 2011.

[31] M.-S. Kwon, J.-S. Shin, S.-Y. Shin, and W.-G. Lee, "Characterizations of realized metal-insulator-silicon-insulator-metal waveguides and nanochannel fabrication via insulator removal," *Opt. Express*, vol. 20, no. 20, pp. 21875–21887, Sep. 2012.

[32] S. Zhu, G. Q. Lo, and D. L. Kwong, "Electro-absorption modulation in horizontal metal-insulator-silicon-insulator-metal nanoplasmonic slot waveguides," *Appl. Phys. Lett.*, vol. 99, no. 15, Oct. 2011, Art. no. 151114.

[33] S. Zhu, G. Q. Lo, and D. L. Kwong, "Performance of ultracompact copper-capped silicon hybrid plasmonic waveguide-ring resonators at telecom wavelengths," *Opt. Express*, vol. 20, no. 14, pp. 15232–15246, Jul. 2012.

[34] Y. Huang, S. Zhu, H. Zhang, T.-Y. Liow, and G.-Q. Lo, "CMOS compatible horizontal nanoplasmonic slot waveguides TE-pass polarizer on silicon-on-insulator platform," *Opt. Express*, vol. 21, no. 10, pp. 12790–12796, May 2013.

[35] M.-S. Kwon and J.-S. Shin, "Investigation of 90° submicrometer radius bends of metal-insulator-silicon-insulator-metal waveguides," *Opt. Lett.*, vol. 39, no. 3, pp. 715–718, Feb. 2014.
[36] B. Ku, J.-S. Shin, and M.-S. Kwon, "Experimental investigation of plasmofluidic waveguides," *Appl. Phys. Lett.*, vol. 107, no. 20, Nov. 2015, Art. no. 201104.
[37] M.-S. Kwon, B. Ku, and Y. Kim, "Plasmofluidic disk resonators," *Sci. Rep.*, vol. 6, Mar. 2016, Art. no. 23149.
[38] G. W. Hanson, "Dyadic Green's functions and guided surface waves for a surface conductivity model of graphene," *J. Appl. Phys.*, vol. 103, no. 6, Mar. 2008, Art. no. 064302.
[39] H. Hu, F. Zhai, D. Hu, Z. Li, B. Bai, X. Yang, and Q. Dai, "Broadly tunable graphene plasmons using an ion-gel top gate with low control voltage," *Nanoscale*, vol. 7, no. 46, pp. 19493–19500, Oct. 2015.
[40] G. Tarabella, F. M. Mohammadi, N. Coppedè, F. Barbero, S. Iannotta, C. Santato, and F. Cicoira, "New opportunities for organic electronics and bioelectronics: Ions in action," *Chem. Sci.*, vol. 4, no. 4, pp. 1395–1409, Dec. 2012.
[41] H.-M. Li, K. Xu, B. Bourdon, H. Lu, Y.-C. Lin, J. A. Robinson, A. C. Seabaugh, and S. K. Fullerton-Shirey, "Electric double layer dynamics in poly(ethylene oxide) $LiClO_4$ on graphene transistors," *J. Phys. Chem. C*, vol. 121, no. 31, pp. 16996–17004, Jul. 2017.
[42] M. J. Panzer and C. D. Frisbie, "Polymer electrolyte-gated organic field-effect transistors: Low-voltage, high-current switches for organic electronics and testbeds for probing electrical transport at high charge carrier density," *J. Amer. Chem. Soc.*, vol. 129, no. 20, pp. 6599–6607, May 2007.
[43] M. K. Vyas and A. Chandra, "Ion–electron-conducting polymer composites: Promising electromagnetic interference shielding material," *ACS Appl. Mater. Interfaces*, vol. 8, no. 28, pp. 18450–18461, Jun. 2016.
[44] S. Bae, H. Kim, Y. Lee, X. Xu, J.-S. Park, Y. Zheng, J. Balakrishnan, T. Lei, H. R. Kim, Y. I. Song, Y.-J. Kim, K. S. Kim, B. Özyilmaz, J.-H. Ahn, B. H. Hong, and S. Iijima, "Roll-to-roll production of 30-inch graphene films for transparent electrodes," *Nature Nanotechnol.*, vol. 5, no. 8, pp. 574–578, Jun. 2010.
[45] J. S. Moon, M. Antcliffe, H. C. Seo, D. Curtis, S. Lin, A. Schmitz, I. Milosavljevic, A. A. Kiselev, R. S. Ross, D. K. Gaskill, P. M. Campbell, R. C. Fitch, K.-M. Lee, and P. Asbeck, "Ultra-low resistance ohmic contacts in graphene field effect transistors," *Appl. Phys. Lett.*, vol. 100, no. 20, May 2012, Art. no. 203512.
[46] Y. Kim and M.-S. Kwon, "Electroabsorption modulator based on inverted-rib-type silicon waveguide including double graphene layers," *J. Opt.*, vol. 19, no. 4, Mar. 2017, Art. no. 045804.
[47] A. Abbas, M. Karabiyik, and N. Pala, "Graphene-based field-effect transistor structures for terahertz applications," *Proc. SPIE*, vol. 8363, May 2012, Art. no. 83630S.
[48] A. Das, S. Pisana, B. Chakraborty, S. Piscanec, S. K. Saha, U. V. Waghmare, K. S. Novoselov, H. R. Krishnamurthy, A. K. Geim, A. C. Ferrari, and A. K. Sood, "Monitoring dopants by Raman scattering in an electrochemically top-gated graphene transistor," *Nature Nanotechnol.*, vol. 3, pp. 210–215, Feb. 2008.
[49] J. A. Robinson, M. Wetherington, J. L. Tedesco, P. M. Campbell, X. Weng, J. Stitt, M. A. Fanton, E. Frantz, D. Snyder, B. L. VanMil, G. G. Jernigan, R. L. Myers-Ward, C. R. Eddy, and D. K. Gaskill, "Correlating Raman spectral signatures with carrier mobility in epitaxial graphene: A guide to achieving high mobility on the wafer scale," *Nano Lett.*, vol. 9, pp. 2873–2876, Jul. 2009.
[50] S. Kim, J. Nah, I. Jo, D. Shahrjerdi, L. Colombo, Z. Yao, E. Tutuc, and S. K. Banerjee, "Realization of a high mobility dual-gated graphene field-effect transistor with $Al_2O_3$ dielectric," *Appl. Phys. Lett.*, vol. 94, no. 6, Feb. 2009, Art. no. 062107.
[51] G. Giovannetti, P. A. Khomyakov, G. Brocks, V. M. Karpan, J. van den Brink, and P. J. Kelly, "Doping graphene with metal contacts," *Phys. Rev. Lett.*, vol. 101, no. 2, Jul. 2008, Art. no. 026803.
[52] A. Varykhalov, M. R. Scholz, T. K. Kim, and O. Rader, "Effect of noble-metal contacts on doping and band gap of graphene," *Phys. Rev. B, Condens. Matter*, vol. 82, no. 12, Sep. 2010, Art. no. 121101.

**YONGHAN KIM** received the B.S. degree in electrical engineering from the Ulsan National Institute of Science and Technology (UNIST), Ulsan, South Korea, in 2014, where he is currently pursuing the Ph.D. degree in electrical engineering. His research interest includes graphene-based nanophotonic devices and plasmonic devices for near-infrared and mid-infrared applications.

**MIN-SUK KWON** received the B.S. *(summa cum laude)*, M.S., and Ph.D. degrees in electrical engineering from the Korea Advanced Institute of Science and Technology (KAIST), Daejeon, South Korea, in 1998, 2000, and 2005, respectively.

He was a Postdoctoral Research Associate with KAIST and the University of Southern California. In September 2007, he joined the Department of Optical Engineering, Sejong University, as a full-time Lecturer. In March 2009, he became an Assistant Professor and worked there, until January 2012. Since January 2012, he has been an Associate Professor with the School of Electrical and Computer Engineering, Ulsan National Institute of Science and Technology (UNIST). He did active researches on thermo-optically induced long-period gratings. He has been studying integrated-optical sensors based on micro-ring resonators, long-period waveguide gratings, and surface plasmon polaritons. In addition, he strongly focuses on the development of nanoplasmonic waveguide devices and graphene-based waveguide devices.